**Proceedings of the ASME 2022 17th International Manufacturing Science and Engineering Conference MSEC2022 June 27 – July 1, 2022 West Lafayette, Indiana, USA**

**MSEC2022-85747**

# ANALYTICAL STUDY OF SHEAR-THINNING FLUID FLOW IN DIRECT INK WRITING PROCESS

**Zipeng Guo**
Department of Industrial and Systems Engineering
University at Buffalo, The State University of New York
Buffalo NY, 14260

**Fan Fei**
Department of Industrial and Systems Engineering
University of Iowa
Iowa City IA, 52242

**Xuan Song**
Assistant Professor
Department of Industrial and Systems Engineering
University of Iowa
Iowa City IA, 52242

**Chi Zhou**[1]
Associate Professor
Department of Industrial and Systems Engineering
University at Buffalo, The State University of New York
Buffalo NY, 14260

## ABSTRACT

*As a facile and versatile additive manufacturing technology, direct ink writing (DIW) has attracted considerable interest in academia and industry to fabricate three-dimensional structures with unique properties and functionalities. Upsurging research endeavors are invested in DIW across many fields to seize the opportunities to create emerging applications. The non-Newtonian shear-thinning inks facilitate the continuous filament extrusion and retain 3D structure after printing, thus being favorable for DIW. The facile ink preparation and easy-accessible to DIW printers offered a platform to create significant achievement from experimental outcomes. However, so far, the physical phenomena during the DIW process are not revealed in detail, leaving a research gap between the physical experiments and the underlying theories. Here, we presented a comprehensive simulation study of non-Newtonian ink flow during the DIW process. The shear-thinning phenomena were revealed in the simulation results and further proved by the experimental validation. In addition, the ink shear stress and velocity fields were demonstrated and compared in the case studies. The advantages and drawbacks of each syringe-nozzle geometry were analyzed. Based on these investigations and analysis, we proposed an optimal syringe-nozzle geometry towards high-resolution DIW. Consequently, the high-resolution and high shape fidelity DIW could enhance the DIW product performance. The results developed in this work offer valuable guidelines and could accelerate further advancement of DIW.*

Keywords: Additive Manufacturing, Direct ink writing, non-Newtonian fluid, shear-thinning, ink flow simulation, computational fluid dynamics, nozzle optimization

## 1. INTRODUCTION

The direct ink writing (DIW) process is one of the most broadly used 3D printing techniques. It is capable of assembling feedstock materials to complex 3D shapes on a digitally defined deposition path. DIW is a versatile and cost-effective additive manufacturing process, offering unparalleled opportunities in fabricating multi-scale and multi-functional products. Although DIW has easy accessibility and the process is straightforward, interests in material variability, shape complexity, printing resolution, and fidelity are continuously leading the development of the DIW process [1]. In fact, the rapid advancement of DIW has been heavily adopted across many research areas and found diverse applications of the printed samples, including energy storage [2], catalyst [3], bone repair [4], artificial organ [5], water purification [6], and thermal insulation [7, 8].

Two factors are of importance for successful DIW, the ink printability and the printing resolution. Printable inks shall possess non-Newtonian shear-thinning property to ensure continuous filament extrusion and maintain the free-standing 3D shape after printing. The unique shear-thinning property depicts the ink viscosity decreases with the increasing shear rate. During the DIW process, forces exert from the syringe inlet, extruding the ink along the axial direction. As the extrusion process proceeds, the shear rate increases with the narrowing space in the syringe and nozzle. The shear stress further elongates the structural units (e.g., untangled polymer chains, stretched fibers, deformed bubbles) within the colloidal inks, and thus originate the shear-thinning behavior. For instance, particle suspension is one of the widely used DIW inks. At a quiescent state, the particles within the ink could be either aggregated due to van der Waals attraction or randomly separated by the repulsive charges on surfaces. In addition, fibers within the ink could orient

[1] Corresponding author: chizhou@buffalo.edu

randomly, following the minimum energy principle. However, when subjected to shear stress, the particles are disintegrated from the particle-particle interaction, and the fibers are stretched along the flow direction. As a result, these changes facilitate the shear flow, thus lowering the viscosity with increasing shear stress [9]. Guo et al. [1] comprehensively summarized the ink composition and the resulting rheology property. A rotary rheometer is often used to characterize the shear-thinning property. However, the viscosity data is not always applicable to inks in the real DIW process. On the other hand, the in-situ and real-time measurement of the viscosity-shear rate relation in DIW is still a challenge. Such investigation cannot be carried out using approaches like the particle imaging velocimetry (PIV). The use of tracing particles does not provide sufficient resolution for numerical studies in three-dimensional. Furthermore, increasing the tracing particle concentration could change the nature of the ink dynamics.

As the computational capability rapidly increases and more empirical models are established, computational fluid dynamics (CFD) becomes a powerful tool to elucidate the physical phenomena during the shear-thinning extrusion process comprehensively. In fact, researchers rely on the simulation results to guide the experimental studies in many applications. The Marsh funnel model was adopted in CFD simulation by Li.et al. [10] to analyze the rheology behavior of non-Newtonian fluids. The wall shear rate, shear stress, and the velocity data were obtained using the CFD model, revealing the flow field inside the Marsh funnel. These results provide essential information for preventing shear-induced degradation during oil drilling operations. Li. M et al. [11] developed CFD models to examine the cell viability with different nozzle geometries used in extrusion-based bio-fabrication. The results found that the conical-shape nozzle is favorable for preventing shear-induced cell damage. The numerical simulation was also employed to study the feasibility of the food DIW process. Yang et al. [12] carried out numerical analysis of the lemon juice gel printing process. The results found that the juice gel is printable, and the inlet volume flow rate is a primary parameter to determine the extrusion velocity field. Besides, the nozzle diameter has a significant influence on the outlet pressure distribution. A similar result was reported by Liu et al. [13]. Guo et al. [14] compared the syringe-based and screw-based food printing process using the computational simulation. It was found that the syringe-based process is favorable for continuous and stable extrusion. On the contrary, an overly high shear rate and backflows were found in the screw-based extrusion, causing discontinued extrusion. Although these results are informative and offer qualitative instructions, the printing resolution is not of major concern in food printing. As a matter of fact, the printing resolution and shape fidelity in both the lateral and vertical direction contribute to acquiring the high performance of the printed samples. Therefore, a comprehensive simulation study of the DIW process is highly desired.

Although CFD methods have been extensively adopted in studying the shear-thinning property of non-Newtonian fluids, however, the studies of non-Newtonian fluid theories are still establishing, and it is far more challenging than that of the typical Newtonian fluid. Consequently, a research gap exists in using numerical simulation to investigate the DIW process. Specifically, the ink velocity change and shear stress variations in the DIW have not been comprehensively revealed. Herein, aiming to investigate and quantify the effects of syringe-nozzle geometry on the ink flow behavior in the DIW process, we employed three types of syringe-nozzle geometries for CFD simulation studies. The conical nozzle, cylindrical nozzle, and conical body with cylindrical tip nozzle are the most widely used configurations in DIW. The shear-dependent viscosity variation was verified by the CFD simulation and validated by the

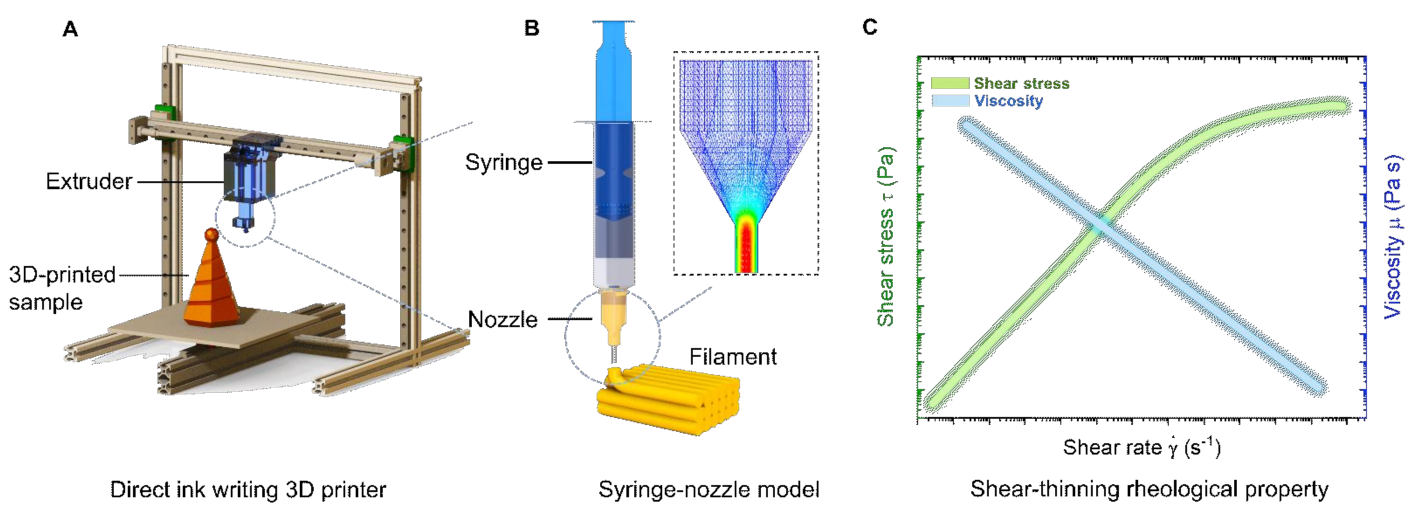


**Figure 1**. (A) Schematic of direct ink writing configuration. (B) A representative syringe-nozzle model for the simulation. (C) The rheological property of non-Newtonian inks.

experimental test. The shear stress and velocity profiles of each syringe-nozzle model were reported and compared. The shear stress and velocity values, distributions, and variations are critical factors towards a stable and high-resolution DIW process.

Furthermore, we found high consistency in our simulation results with both our and other published experimental studies. To the best of our knowledge, our work is the first comprehensive physics-based simulation study dedicated to demonstrating the shear-thinning ink property and comparing the ink flow behavior in different syringe-nozzle geometries. Moreover, we examined the strengths and weaknesses of each syringe-nozzle model. Based on these comparative studies, we proposed an optimal solution towards high-resolution and high shape fidelity DIW. The CFD methods are explained in section 2. Section 3 presents the simulation case studies. An in-depth and comprehensive discussion is detailed in Section 4.

## 2. METHODS

### 2.1 Material property

A printable ink for the extrusion 3D printing is usually formulated as a shear-thinning fluid to ensure continuous filament-extrusion. The ink could be a single-phase solution or multi-phase particle suspensions and oil-water emulsions. The materials used in this simulation study can be described as a single fluid exhibiting non-Newtonian rheological behavior. The viscosity of non-Newtonian ink is a function of the local shear (deformation) rate, which contains shearing and elongations. The Herschel-Bulkley model can be used to approximate the relation between shear rate ($\dot{\gamma}$) and viscosity (η), given by:

$$\eta = \frac{\tau_{yield}}{\dot{\gamma}} + k\dot{\gamma}^{n-1} \tag{1}$$

The shear rate is defined as:

$$\dot{\gamma} = \sqrt{\frac{1}{2}\overline{\overline{\boldsymbol{D}}}:\overline{\overline{\boldsymbol{D}}}} = \sqrt{\frac{1}{2}\sum_{ij}\overline{\overline{\boldsymbol{d}}}_{ij}\overline{\overline{\boldsymbol{d}}}_{ij}} \tag{2}$$

Where $\overline{\overline{\boldsymbol{D}}}$ is a tensor of deformation rate and given by:

$$\overline{\overline{\boldsymbol{D}}} = (\frac{\partial u_j}{\partial x_i} + \frac{\partial u_i}{\partial x_j}) \tag{3}$$

The yield stress $\tau_{yield}$ is the shear stress at zero shear rate. $k$ is the consistency coefficient that measures the average viscosity. $n$ is the flow index which is a measure of deviation from a Newtonian fluid. When $0 < n < 1$, the ink is a non-Newtonian fluid. The more significant shear-thinning of ink, the closer $n$ is to 0. In addition, when $n = 1$, viscosity becomes a constant value, denoting a typical Newtonian fluid. In practice, it was found that when $n \geq 0.8$, inks behave as a Newtonian fluid [15]. The parameter used in the simulation were collected from several references and were summarized in table 1.

### 2.2 Computational fluid dynamics (CFD) simulation

The incompressible fluids were adopted in the simulation models based on the Eulerian approach. By enforcing the conservation of mass, the convection of mass through the system shall equal the mass accumulation within the system. Thus, the continuity equation of the ink flow is expressed as follows:

$$\frac{\partial \rho}{\partial t} = -\nabla(\rho\vec{u}) \tag{4}$$

where ρ is the fluid density (kg m$^{-3}$), and $\vec{u}$ is the velocity vector.

The ink flow was governed by the Navier-Stokes equations, with modified terms for complement the non-linear rheology effects, expressed as follows [16, 17]:

$$\frac{\partial(\rho v_i)}{\partial t} + \sum_j \frac{\partial(\rho v_i v_j)}{\partial x_j} = \sum_j \frac{\partial \sigma_{ij}}{\partial x_j} + \rho f_i \tag{5}$$

where $v_i$ (index notation) are the velocity components, and $f$ is the body force. $\hat{\boldsymbol{\sigma}} = (\sigma_{ij})$ denotes the stress tensor, it can be described as:

$$\sigma_{ij} = -p\delta_{ij} + \eta(\frac{\partial v_i}{\partial x_j} + \frac{\partial v_j}{\partial x_i}) \tag{6}$$

In this case, $\mu$ denotes the fluid viscosity. For a non-Newtonian fluid, the viscosity is a function of the shear rate (equation (1)) as introduced in section 2.1.

The standard $k - \varepsilon$ method, proposed by Launder and Spalding (1972), is an empirical model based on the transportation equations for the turbulent kinetic energy (k, equation (7)) and the dissipation rate ($\varepsilon$, equation (8)). This model was adopted for all the following case studies since it is shown to better handle low-Reynolds-number and near-wall flows [18, 19].

$$\frac{\partial \rho k}{\partial t} + \frac{\partial \rho k u_i}{\partial x_i} = \frac{\partial}{\partial x_j}\left[(\mu + \frac{\mu_t}{\sigma_k})\frac{\partial k}{\partial x_j}\right] + G_k + G_B - \rho\varepsilon + S_k \tag{7}$$

$$\frac{\partial \rho \varepsilon}{\partial t} + \frac{\partial \rho \varepsilon u_i}{\partial x_i} = \frac{\partial}{\partial x_j}\left[(\mu + \frac{\mu_t}{\sigma_\varepsilon})\frac{\partial \varepsilon}{\partial x_j}\right] + C_{1\varepsilon}\varepsilon k(G_k + C_{3\varepsilon}G_B) - C_{2\varepsilon}\rho(\frac{\varepsilon^2}{k}) \tag{8}$$

$\sigma_k$ and $\sigma_\varepsilon$ are the inverse value of Prandtl numbers for $k$ and $\varepsilon$, respectively. $G_k$ marks the generation of kinetic energy due to the mean velocity gradients. $G_k$ denotes the generation of kinetic energy due to buoyancy. $C_{1\varepsilon} = 1.44$, $C_{2\varepsilon} = 1.92$, $C_{3\varepsilon} = -0.33$, $\sigma_k = 1.0$, and $\sigma_\varepsilon = 1.3$ are model-specific constants (Launder and Spalding).

The wall shear stress can be derived from the Herschel-Bulkley model [20], given by:

$$\tau_{wall} = \tau_{yield} + K\dot{\gamma}_{wall}{}^n \tag{9}$$

**Table 1 Summary of material properties and simulation parameters**

| Parameter | Notation | Unit | Value | Reference |
|---|---|---|---|---|
| Density | $\rho$ | kg m$^{-3}$ | 1240 | [10, 21, 22] |
| Consistency coefficient | k | Pa s | 568.6 | [23, 24] |
| Flow index | n | - | 0.335 | [23-25] |
| Yield stress | $\tau_{yield}$ | Pa | 764.01 | [8, 26-29] |

### 2.3 Syringe-nozzle model

Three types of syringe-nozzle geometries were incorporated for the case studies, namely conical nozzle, cylindrical nozzle, and conical body with cylindrical tip nozzle, with nozzle orifice diameter of 0.6 mm for all case studies. These three types are the most common geometries used in the literature. Due to the axisymmetric structure of syringes and nozzles, many literatures utilized 2D model [22, 30-32] or half-plane model [26] for faster convergence and reduced calculation complexity. However, we specifically constructed 3D CAD for demonstrating the dynamic viscosity change, ink flow velocity, and wall shear stress. The 3D structured mesh was assembled using the sweep-axisymmetric method with hexahedra grids in the center. This algorithm guarantees that the simulation result does not deviate at the nozzle region where the cross-section is small compared to the syringe body. We also performed convergence studies to verify the grid independence of the results. Based on the convergence study, the element (grid) size was set at 0.05 mm, and the skewness of 0.39. The total elements of the structured mesh are 1254084 with 5045659 nodes for the cylindrical nozzle model.

The constant pressure (5 psi) condition was imposed at the syringe inlet for all the models. The normal and axial forces at the outlet were set at zero for all the case studies. The wall was subjected to no-slip boundary conditions.

### 2.4 Rheological characterization

The rheological characterization was carried out to verify the shear-thinning properties of the ink flow used in the simulation. We prepared three printable inks for the rheological tests, including the silica aerogel-based ink, the silicon dioxide-based ink, and the alumina-based ink. All the inks were prepared using previously published protocol [33].

The rheological behavior of the printable ink was characterized at room temperature using a rotational rheometer (Anton Paar MCR 72, Ashland, VA). The measurement setup was equipped with a parallel plate-plate geometry. The diameter of the plates is 25 mm, with a 1 mm gap in between. The apparent viscosity measurement was performed at a shear rate that ranged from $10^{-2}$ to $10^{2}$ s$^{-1}$.

## 3 RESULTS

### 3.1 Viscosity profile and shear-thinning behavior

As outlined in the introduction section, during extrusion printing, pressure is exerted at the inlet of the syringe, forcing the ink to flow along the longitudinal direction (z-axis in Figure 1) of the syringe. We divide the syringe-nozzle model into three regions for analyzing the following simulation results. Region 1 denotes the flow inlet area. Region 2 is the syringe body with a simple cylindrical geometry. Region 3 describes the nozzle outlet area.

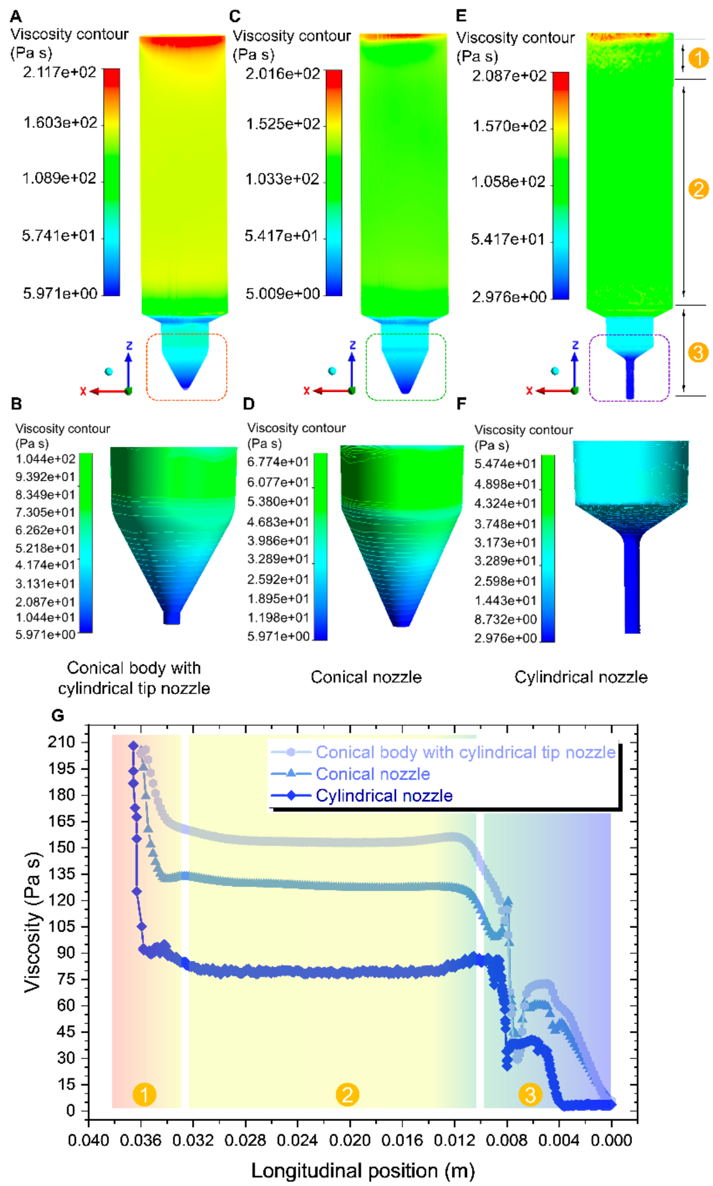


**Figure 2**. Viscosity contours of (A-B) The conical body with cylindrical tip nozzle. (C-D) The conical nozzle. (E-F) The

cylindrical nozzle. (G) Apparent viscosity plots of each syringe-nozzle geometry. The longitudinal position refers to the position along the z-axis in the figures.

Figure 2 shows the simulated result of ink viscosity profiles. In general, high viscosity was observed at the inlet area, where the shear deformation was small. A more significant shear deformation occurs at the position below the inlet area, leading to a sharply decreased viscosity (as shown at the interface of regions 1 and 2). At region 2 the ink viscosity reaches an equilibrium state as indicated by the uniform color, denoting the flow shear rate ($\dot{\gamma}$) remains constant. As the syringe-nozzle geometry necks down at the outlet region, the viscosity again decreases sharply (refer to the interface of regions 2 and 3). The lowest viscosity appears at the nozzle tip, where the shear rate is the largest and radial dimensional is the smallest. In addition, we observed that cylindrical nozzle tip (Figures 2 (B) and (F)) tends to have a stabilized ink viscosity, which would be beneficial for acquiring uniform extrusions. The viscosity contours in Figure 1 clearly reveal the "shear-thinning" property of the non-Newtonian ink. When the ink flow experiences the shear deformation, it becomes thinner than that in the quiescent state. The term "Apparent Viscosity (Pa s)" is more often used to describe the shear-dependent viscosity or used as a measure of resistance to the shear deformation of such non-Newtonian fluids.

### 3.2 Shear stress

Understanding the flow shear stress during extrusion is vital in many engineering fields. Low shear stress is favorable in biomedical applications for avoiding shear degradation. In contrast, high shear stress could be beneficial to enhance the sample properties after extrusion printing. Figure 3 reveals the shear stress changes during extrusion. The shear stress is low in the inlet area, then quickly increases and remains stable at the syringe body regions. Finally at the narrower nozzle region, the shear stress again quickly increases and reaches the maximum value at the nozzle tip. From the color contour, we can see that the shear stress can be stabilized within the cylindrical tips (Figures 3 (B) and (F)), this trend is consistent with the viscosity results. Figure 3 (G) presents the curves of shear stress values along the longitudinal direction. It is worth noting that the cylindrical nozzle has more prominent stress at the nozzle tip than the other cases. This finding provides valuable guidance for the syringe-nozzle design. The high shear stress could facilitate the alignment of filler materials such as rod-like fibers [34, 35] and 2D materials like graphene [27, 36] during the extrusion 3D printing. By aligning the filler materials in the axial direction, it enhances properties such as mechanical strength, electrical conductivity, and thermal insulation. Conversely, low shear stress could be critical to bioprinting to ensure the cell viability, which is a measure of live and healthy cells within the ink [32, 37, 38]. Overly high stress could lead to severely degraded cell viability. In this case, the conical nozzle or the conical nozzle with cylindrical tip nozzle would be ideal tools.

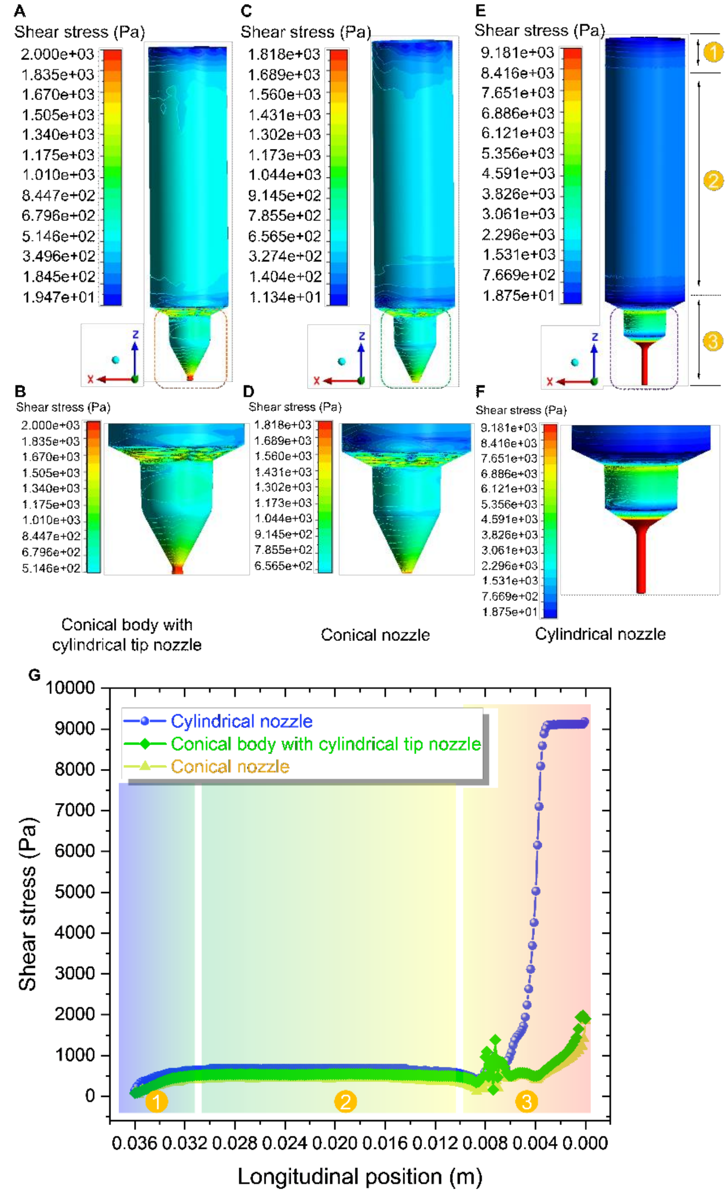


**Figure 3**. Viscosity contours of (A-B) The conical body with cylindrical tip nozzle. (C-D) The conical nozzle. (E-F) The cylindrical nozzle. (G) Shear stress plots of each syringe-nozzle geometry.

### 3.3 Velocity profile

The velocity contours at the cross-sectional plane (x-z plane) are shown in Figure 4, and the velocity profiles were summarized in Figure 5. The velocity at the outlet region is instructive for calibrating the extrusion printing parameters (e.g., printing speed). We noticed that velocity could be stabilized within the cylindrical tips (Figures 4 (C), 4(I), and 5), this trend is consistent with the viscosity and shear stress results. The stabilized ink velocity at the nozzle is critical to ensure the uniform extrusion and the high fidelity of the 3D-printed specimen.

Unstable velocity variations were exhibited at the interface of regions 2 and 3 in the conical body with cylindrical tip nozzle and the conical nozzle (shown in Figures 4 (B) and (E)). These variations lead to locally sudden-increased velocity and the asymmetric velocity distribution. The reason could be linked to the acute necking of the model geometry. Considering this abnormal variation, we further examined the shear stress values within the necking region and concluded that a "dead zone" may exist as a result of the acute necking geometry. The ink flow is aggregated within the "dead zone", resulting in a locally increased shear stress and velocity. On the other hand, such local variation was not observed in the cylindrical nozzle (refer to Figures 3 (F), 4 (H), and (I)). In this case, considerably large shear stress (5-6 times greater than other cases) was presented in the cylindrical nozzle. The large shear stress facilitates the flow and thus eliminates the flow aggregation. A similar result was also reported by Shao et al. [26]. This finding is instructive for our study to design an optimized model for uniform extrusion (in section 3.5). Our previous work [33] conducted a comparative experimental study using three types of nozzles for extrusion printing. We found that the conical body with cylindrical tip nozzle has the most uniform extrusion and thus ensures the best fidelity of printed parts. The result was also consistent with the simulation studies as we presented in this work.

The outlet velocity value and contours were summarized in Figure 6. From the contours, we observed that the center velocity has a plateau region, and gradually decreases to the periphery. The decreasing velocity from the inner area to the outer is because the model was subjected to the no-slip boundary condition, denoting the periphery velocity shall be zero. In this regard, a gradually decreased velocity from the core to the periphery would be preferable. Furthermore, a greater percentage of the plateau region is favorable for extruding the cylindrical-shape filament, ensuring the high printing resolution. The simulated plateau velocity has the value of 5 mm $s^{-1}$ to 10 mm $s^{-1}$, which is consistent with our previous experimental studies [7] and other published works [28, 30, 39-41].

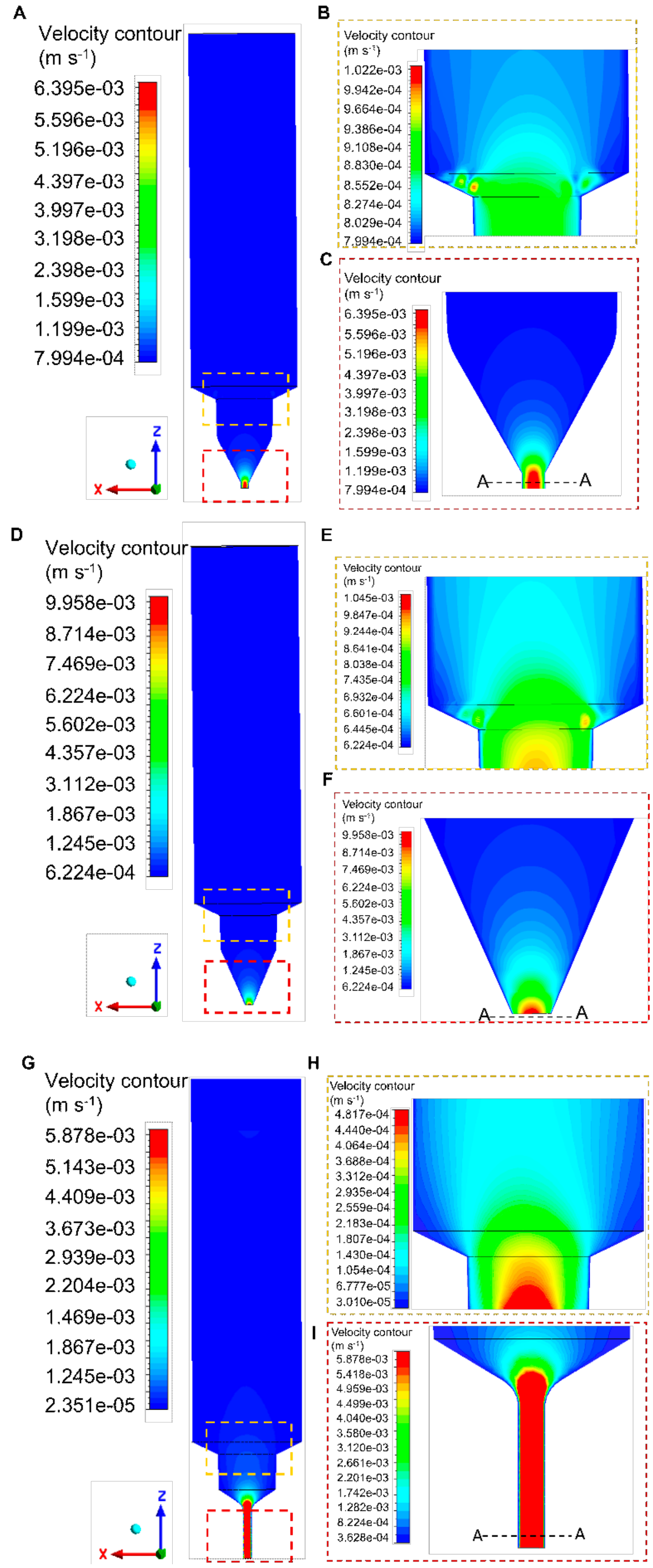

**Figure 4**. Velocity contours of (A-C) The conical body with cylindrical tip nozzle. (D-F) The conical nozzle. (G-I) The cylindrical nozzle.

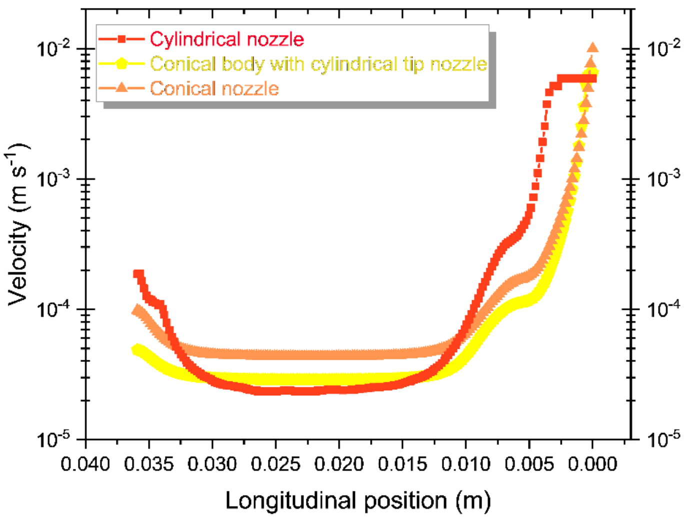


**Figure 5**. Velocity profiles (along the central axis, at x=0) of each syringe-nozzle geometry. The longitudinal position refers to the position along the z-axis.

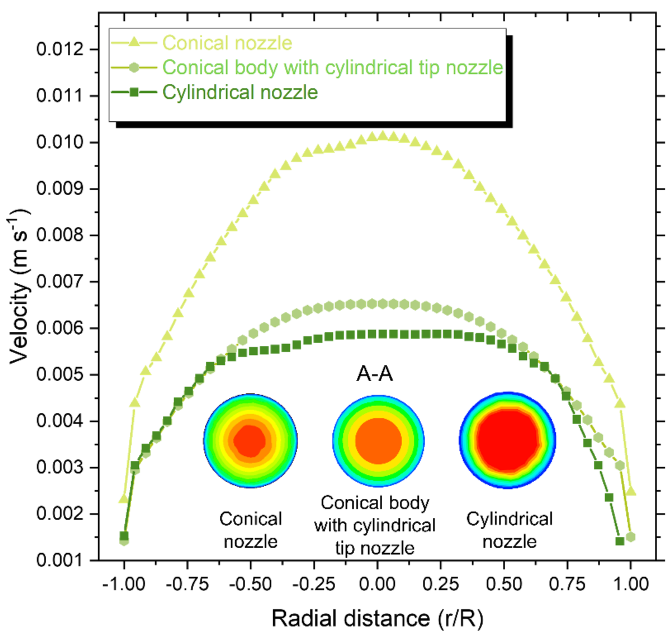


**Figure 6**. Velocity plots at the nozzle outlet of each syringe-nozzle geometry. The radial distance refers to the position along the x-axis in figure 4.

### 3.4 Experimental validation

We performed the rheology measurements for the ceramic inks with silica aerogel, alumina, and silica nanoparticle, respectively. The apparent viscosity (Pa s) was plotted against the shear rate ($s^{-1}$) in Figure 7. The curves show all the inks exhibit the shear-thinning behavior under shear stress, as evidenced by a rapid decrease in the apparent viscosity with respect to the increasing shear rate from $10^{-2}$ to $10^{2}$ $s^{-1}$.

Physically, the apparent viscosity during the extrusion is very low, and ink exhibits typical fluid-like behavior. The viscosity is thinned to be low enough for the continuous filament extrusion. Upon exiting the nozzle, as shear deformation vanishes, the apparent viscosity increases and instantly recovers the elastic (solid-like) behavior. Therefore, the ink can form and maintain the self-supported 3D shape without wetting or spreading during the direct ink writing process.

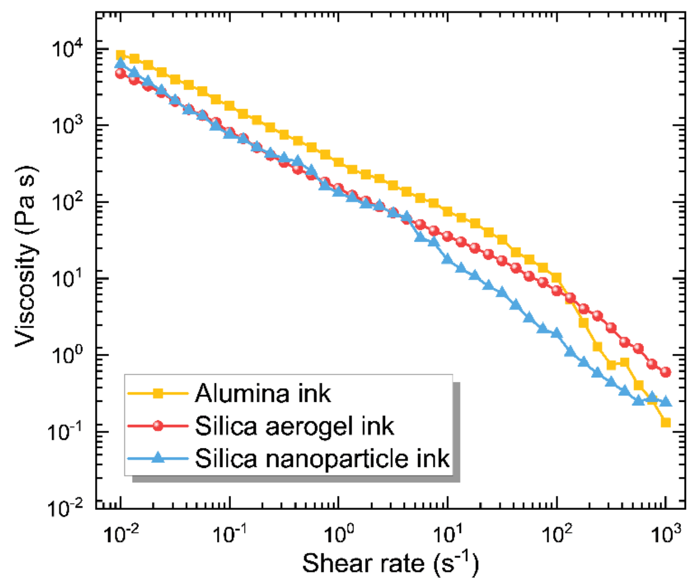


**Figure 7**. Rheology measurement results: The apparent viscosity as a function of shear rate.

### 3.5 Optimal nozzle design

The aforementioned case studies provided a valuable comparison of each syringe-nozzle model. Based on the simulation case studies, it can be summarized that with a cylindrical tip at the nozzle outlet, the ink velocity and shear stress can be stabilized, providing a favorable condition for high-resolution printing. On the other hand, the sharp geometry change could lead to locally fluctuated flow and should be addressed. We summarized the detailed pros and cons in Table 2.

In light of the comparison, we proposed an optimal solution to integrate the merits from each model and optimize the geometry to eliminate the unsteady flow. Specifically, the optimization targets are (1) eliminate the "dead zone" area to create smooth ink flow at the syringe necking region. (2) Maintain the steady velocity at the outlet and reduce the shear stress at the tip.

The proposed model extended the basic geometry of the conical body with cylindrical tip nozzle. The original sharp edges at the syringe necking region were changed to curved and smoothly converged edges (Figure 8(A)). The tip length was elongated from 1 mm to 2.5 mm. The simulated velocity results were shown in Figure 8. The contour (Figures 8 (A) – (C)) and the profile ((D) and (E)) revealed no unsteady flows throughout the entire model. The curved edge facilitates the ink flow by mitigating the stress concentration, and the velocity can gradually increase at the necking region and nozzle region. In addition, steady velocity holds at the nozzle outlet. Together with the shear stress results in Figure 9, it shows the "dead zone" area was eliminated on the proposed model. The maximum shear stress was much lower than the cylindrical nozzle and marginally higher than the other two cases. This optimal solution could be further applied to multi-nozzle and multi-material 3D printing, where the stable extrusion behavior is at the heart of these research areas [42].

**Table 2 Comparison between different nozzles**

| Model | Shear stress | | Velocity | |
|---|---|---|---|---|
| | Pros | Cons | Pros | Cons |
| Cylindrical nozzle | Stable shear stress within the long nozzle region | Shear stress value is much higher than the other cases | Stable velocity within the long nozzle region. Outlet velocity has larger plateau region | - |
| Conical body with cylindrical tip nozzle | Stable shear stress within the nozzle region | "Dead zone" appeared at the syringe necking area | Stable velocity within the nozzle region | Small plateau region on the outlet velocity profile |
| Conical nozzle | - | "Dead zone" appeared at the syringe necking area | - | Small plateau region on the outlet velocity profile |

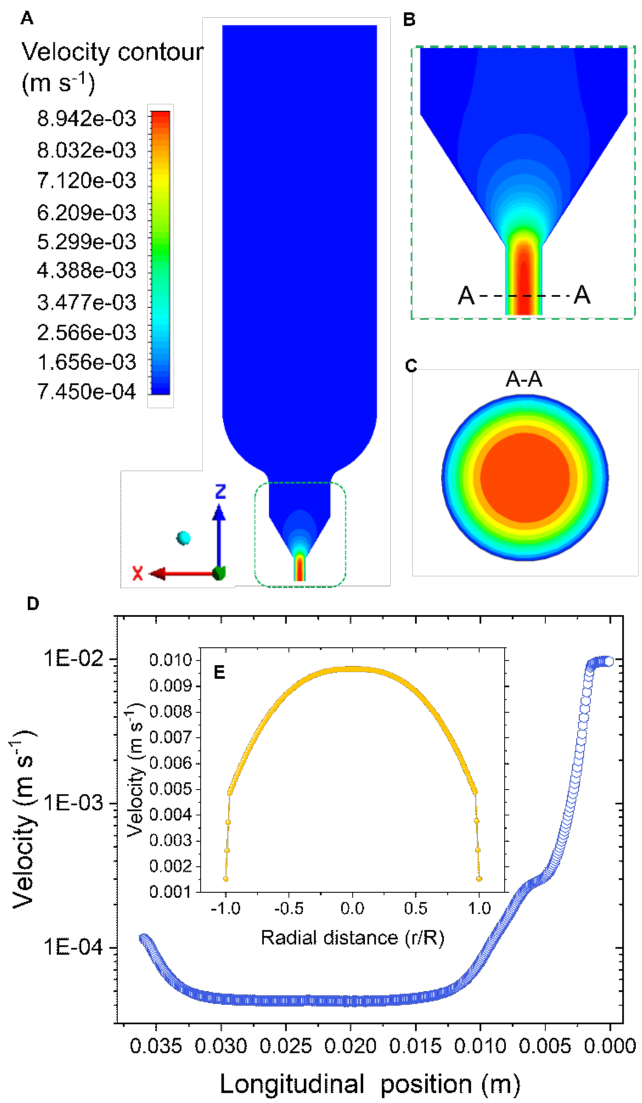


**Figure 8**. Simulated velocity results of the proposed optimal model. (A) Velocity contour of the optimal syringe-nozzle model. (B) Close-up view of the nozzle outlet region. (C) Cross-sectional velocity contour of the nozzle outlet. (D) Velocity profile along the longitudinal direction. (E) nozzle outlet velocity profile.

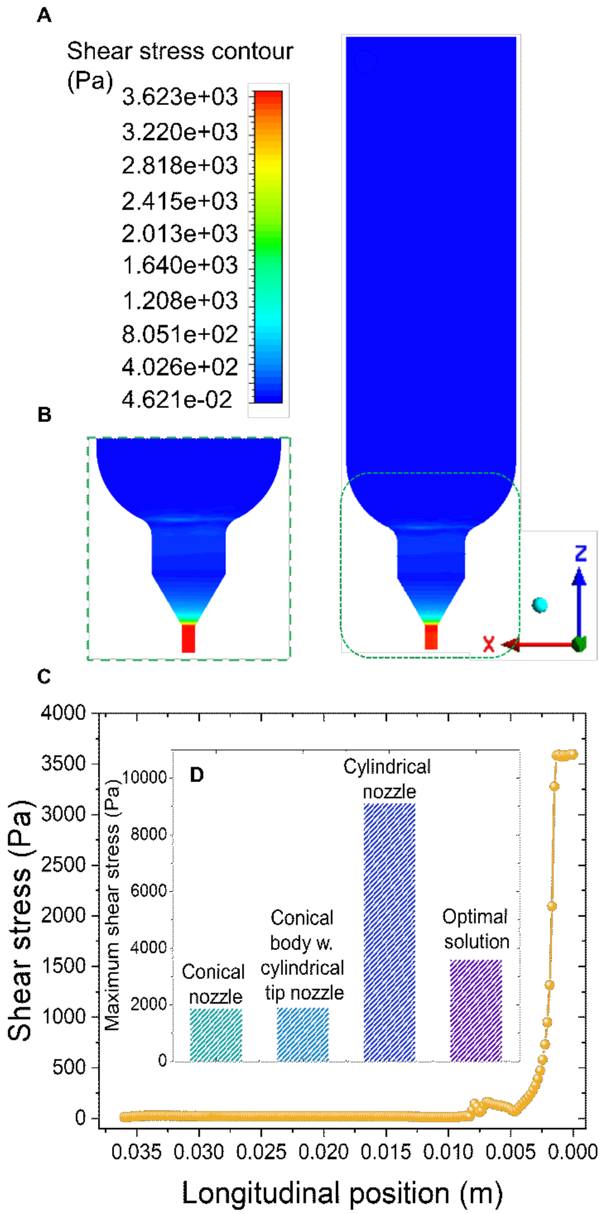


**Figure 9**. Simulated shear stress results of the proposed optimal model. (A) Shear stress contour of the optimal syringe-nozzle model. (B) Close-up view of the nozzle outlet region. (C) Shear stress profile along the longitudinal direction. (D) A summary of the maximum shear stress of each model.

## 3. DISCUSSION

In practice, the three types of syringe-nozzle models included in our simulation study were widely used for the 3D direct ink writing (DIW) process. Pilot DIW works by Lewis et al. [43-46] employed the cylindrical nozzles for DIW. As this field rapidly developed, the low-cost conical nozzles made from plastics are becoming popular [28, 47, 48]. On the contrary, the conical body with cylindrical nozzles is costly, but it could play a vital role in high-resolution DIW [8, 33]. Recently, as more research endeavors were invested and methodologies went deeper, the attention has been directed toward the DIW resolution and fidelity. The high-resolution and high shape fidelity 3D printing assembles the feedstock materials to continuous and conformal 3D structures. Consequently, it ensures a more promising performance, such as electron transfer, energy storage, thermal conductivity, and optical transmittance of the printed specimen [1]. For example, Chortos et al. [49] presented multi-nozzle DIW for soft and flexible dielectric elastomer actuators, possessing significant high energy densities and fast actuation rates. The printing fidelity is particularly important since any defects could cause thinning dielectric segments that reduce the breakdown field when bending or folding the devices. In this regard, the outcomes of this work could serve as an informative guide for experimental studies in the following two aspects.

(1) Understanding the ink flow behavior during DIW and selecting the appropriate nozzle geometry accordingly. For example, from our comparative simulations, we learned that the conical nozzle and conical body with cylindrical tip nozzle have low shear stress. Shear stress is a major contributing factor in cell viability during 3D bioprinting. It is therefore making the conical nozzles favorable candidates to maximize the cell viability. On the other hand, high shear stress could present on the cylindrical nozzle, generating a favorable condition for aligning the 2D filler materials (e.g., fiber) in ink. The orientation of fibers within a composite is a significant factor that defines the ultimate strength. When subjected to high shear stress, the fibers can overcome the random orbital rotation and align in the flow direction [50]. This mechanism also works with other 2D materials such as graphene, boron nitride, and MXenes. Additionally, the nozzles with cylindrical tips have stable extrusion shear stress and velocity at the outlet. Thus, it can be used to precisely control the printing resolution and shape fidelity. Moreover, the velocity at the nozzle outlet can be referenced for defining the printing speed, an essential value that shall be specified while slicing the CAD model, saving efforts for the time-consuming trial-and-error process.

(2) Identify the potential "dead zone" area in the model and propose the optimal geometry towards stable and high-resolution printing. As shown in section 3.3, the dead zone appears at the syringe necking region. However, it could be eliminated by changing the shape corner to curved corner in the proposed model. In fact, avoiding the dead zone has more valuable meaning for physical experiments, primarily because most of the fluids used for DIW are multi-phase fluids [1], such as particle suspensions [7, 28, 33, 35, 46], fiber-induced suspensions [27, 36, 51], oil-water emulsions [52, 53], and foamed inks [7, 33, 54]. The different phase materials may not be uniformly dispersed within the ink, or the uniformity degraded during extrusion. In such cases, any un-uniformity could lead to unsteady flow, resulting in clogging issues at the "dead zone" area and inconsistent ink dispensing as the DIW process progresses. The stable extrusion is even more pivotal when deploying DIW for large-scale 3D printing. A larger printing scale increases the likelihood of shape deviation from

 

the pre-defined model caused by unstable or ununiform extrusion. Therefore, the proposed optimal solution is a promising candidate for stable and high-resolution DIW.

## 4. CONCLUSION

In summary, we conducted the CFD simulation of shear-thinning inks in the DIW process. The results reveal the ink flow behavior throughout the syringe-nozzle model. Specifically, the comparative case studies demonstrate the ink shear stress and flow velocity in three different syringe-nozzle geometries. Furthermore, we found high consistency of our simulation results to the experimental results. Evidenced by the rheology tests to prove the shear-thinning property of the DIW ink. In addition, we found the simulated outlet velocity is consistent with the value used in physical experiments. The results offer readers instructive guidance on selecting the nozzle type for specific DIW processes, economizing the efforts of preliminary trail-and-error experiments. Moreover, we identified the "dead zone" that could cause flow clogging. Based on the findings, we proposed the optimal solution towards high-resolution and high shape fidelity DIW, leading to enhanced performance of the printed samples. We believe the simulation results discussed here can motivate further developments of the direct ink writing process.

## ACKNOWLEDGMENTS

The authors would like to gratefully acknowledge the support from the U.S. Department of Energy (DOE), Office of Energy Efficiency and Renewable Energy (EERE) through the award DEEE-0008675 and the U.S. National Science Foundation (NSF) through the award CMMI-1846863.

## REFERENCES

1. Guo, Z. and C. Zhou, *Recent Advances in Ink-Based Additive Manufacturing for Porous Structure.* Additive Manufacturing, 2021: p. 102405 DOI: 10.1016/j.addma.2021.102405.
2. Zhang, F., M. Wei, V.V. Viswanathan, B. Swart, Y. Shao, G. Wu, and C. Zhou, *3D printing technologies for electrochemical energy storage.* Nano Energy, 2017. **40**: p. 418-431 DOI: 10.1016/j.nanoen.2017.08.037.
3. Zhu, C., Z. Qi, V.A. Beck, M. Luneau, J. Lattimer, W. Chen, M.A. Worsley, J. Ye, E.B. Duoss, and C.M. Spadaccini, *Toward digitally controlled catalyst architectures: Hierarchical nanoporous gold via 3D printing.* Science advances, 2018. **4**(8): p. eaas9459 DOI: 10.1126/sciadv.aas9459.
4. Maroulakos, M., G. Kamperos, L. Tayebi, D. Halazonetis, and Y. Ren, *Applications of 3D printing on craniofacial bone repair: A systematic review.* Journal of Dentistry, 2019. **80**: p. 1-14 DOI: 10.1016/j.jdent.2018.11.004.
5. Bektas, C.K. and V. Hasirci, *Cell loaded 3D bioprinted GelMA hydrogels for corneal stroma engineering.* Biomaterials science, 2020. **8**(1): p. 438-449 DOI: 10.1039/C9BM01236B
6. Coppola, B., C. Tardivat, S. Richaud, J.-M. Tulliani, L. Montanaro, and P. Palmero, *3D printing of dense and porous alkali-activated refractory wastes via Direct Ink Writing (DIW).* Journal of the European Ceramic Society, 2021. **41**(6): p. 3798-3808 DOI: 10.1016/j.jeurceramsoc.2021.01.019.
7. Guo, Z., R. Yang, T. Wang, L. An, S. Ren, and C. Zhou, *Cost-Effective Additive Manufacturing of Ambient Pressure-Dried Silica Aerogel.* Journal of Manufacturing Science and Engineering, 2021. **143**(1): p. 011011 DOI: 10.1115/1.4048740.
8. Zhao, S., G. Siqueira, S. Drdova, D. Norris, C. Ubert, A. Bonnin, S. Galmarini, M. Ganobjak, Z. Pan, and S. Brunner, *Additive manufacturing of silica aerogels.* Nature, 2020. **584**(7821): p. 387-392 DOI: 10.1038/s41586-020-2594-0.
9. Xu, X., S.A. Rice, and A.R. Dinner, *Relation between ordering and shear thinning in colloidal suspensions.* Proceedings of the National Academy of Sciences, 2013. **110**(10): p. 3771-3776 DOI: 10.1073/pnas.1301055110.
10. Li, Z., L. Zheng, and W. Huang, *Rheological analysis of Newtonian and non-Newtonian fluids using Marsh funnel: Experimental study and computational fluid dynamics modeling.* Energy Science & Engineering, 2020. **8**(6): p. 2054-2072 DOI: 10.1002/ese3.647.
11. Li, M., X. Tian, D.J. Schreyer, and X. Chen, *Effect of needle geometry on flow rate and cell damage in the dispensing-based biofabrication process.* Biotechnology progress, 2011. **27**(6): p. 1777-1784 DOI: 10.1002/btpr.679.
12. Yang, F., C. Guo, M. Zhang, B. Bhandari, and Y. Liu, *Improving 3D printing process of lemon juice gel based on fluid flow numerical simulation.* Lwt, 2019. **102**: p. 89-99 DOI: 10.1016/j.lwt.2018.12.031.
13. Liu, Q., N. Zhang, W. Wei, X. Hu, Y. Tan, Y. Yu, Y. Deng, C. Bi, L. Zhang, and H. Zhang, *Assessing the dynamic extrusion-based 3D printing process for power-law fluid using numerical simulation.* Journal of Food Engineering, 2020. **275**: p. 109861 DOI: 10.1016/j.jfoodeng.2019.109861.
14. Guo, C.-F., M. Zhang, and B. Bhandari, *A comparative study between syringe-based and screw-based 3D food printers by computational simulation.* Computers and Electronics in Agriculture, 2019. **162**: p. 397-404 DOI: 10.1016/j.compag.2019.04.032.
15. Chhabra, R.P. and J.F. Richardson, *Non-Newtonian flow and applied rheology: engineering applications*. 2011: Butterworth-Heinemann.
16. Sváček, P., *On approximation of non-Newtonian fluid flow by the finite element method.* Journal of computational and applied mathematics, 2008. **218**(1): p. 167-174 DOI: 10.1016/j.cam.2007.04.040.

 

17. Guo, B. and C. Guo, *The convergence of non-Newtonian fluids to Navier–Stokes equations.* Journal of mathematical analysis and applications, 2009. **357**(2): p. 468-478 DOI: 10.1016/j.jmaa.2009.04.027.
18. Rezaeimoghaddam, M., R. Elahi, M.R. Modarres Razavi, and M.B. Ayani. *Modeling of non-Newtonian fluid flow within simplex atomizers*. in *Engineering Systems Design and Analysis*. 2010. DOI: 10.1115/ESDA2010-25266.
19. Nguyen, V., S. Rémond, J. Gallias, J. Bigas, and P. Muller, *Flow of Herschel–Bulkley fluids through the Marsh cone.* Journal of non-newtonian fluid mechanics, 2006. **139**(1-2): p. 128-134 DOI: 10.1016/j.jnnfm.2006.07.009.
20. Sahu, K., P. Valluri, P. Spelt, and O. Matar, *Linear instability of pressure-driven channel flow of a Newtonian and a Herschel-Bulkley fluid.* Physics of Fluids, 2007. **19**(12): p. 122101 DOI: 10.1063/1.2814385.
21. Hosseini, S., M. Manzari, and S. Hannani, *A fully explicit three-step SPH algorithm for simulation of non-Newtonian fluid flow.* International Journal of Numerical Methods for Heat & Fluid Flow, 2007 DOI: 10.1108/09615530710777976.
22. De Gruttola, S., K. Boomsma, and D. Poulikakos, *Computational simulation of a non-Newtonian model of the blood separation process.* Artificial organs, 2005. **29**(12): p. 949-959 DOI: 10.1111/j.1525-1594.2005.00164.x.
23. Reina-Romo, E., S. Mandal, P. Amorim, V. Bloemen, E. Ferraris, and L. Geris, *Towards the experimentally-informed in silico nozzle design optimization for extrusion-based bioprinting of shear-thinning hydrogels.* Frontiers in bioengineering and biotechnology, 2021: p. 694 DOI: 10.3389/fbioe.2021.701778.
24. Burrell, G.L., N.F. Dunlop, and F. Separovic, *Non-Newtonian viscous shear thinning in ionic liquids.* Soft Matter, 2010. **6**(9): p. 2080-2086 DOI: 10.1039/B916049N.
25. Wu, B. and S. Chen, *CFD simulation of non-Newtonian fluid flow in anaerobic digesters.* Biotechnology and bioengineering, 2008. **99**(3): p. 700-711 DOI: 10.1002/bit.21613.
26. Shao, Y., R. Han, X. Quan, and K. Niu, *Study on ink flow of silicone rubber for direct ink writing.* Journal of Applied Polymer Science, 2021. **138**(33): p. 50819 DOI: 10.1002/app.50819.
27. Liang, Z., Y. Pei, C. Chen, B. Jiang, Y. Yao, H. Xie, M. Jiao, G. Chen, T. Li, and B. Yang, *General, vertical, three-dimensional printing of two-dimensional materials with multiscale alignment.* ACS nano, 2019. **13**(11): p. 12653-12661 DOI: 10.1021/acsnano.9b04202.
28. Muth, J.T., P.G. Dixon, L. Woish, L.J. Gibson, and J.A. Lewis, *Architected cellular ceramics with tailored stiffness via direct foam writing.* Proceedings of the National Academy of Sciences, 2017. **114**(8): p. 1832-1837 DOI: 10.1073/pnas.1616769114.
29. Wang, L., J. Feng, Y. Luo, Z. Zhou, Y. Jiang, X. Luo, L. Xu, L. Li, and J. Feng, *Three-Dimensional-Printed Silica Aerogels for Thermal Insulation by Directly Writing Temperature-Induced Solidifiable Inks.* ACS Applied Materials & Interfaces, 2021. **13**(34): p. 40964-40975 DOI: 10.1021/acsami.1c12020.
30. Sodupe Ortega, E., A. Sanz-Garcia, and C. Escobedo-Lucea, *Efficient fabrication of polycaprolactone scaffolds for printing hybrid tissue-engineered constructs.* Materials, 2019. **12**(4): p. 613 DOI: 10.3390/ma12040613.
31. Latz, M.I., A.R. Juhl, A.M. Ahmed, S.E. Elghobashi, and J. Rohr, *Hydrodynamic stimulation of dinoflagellate bioluminescence: a computational and experimental study.* Journal of experimental biology, 2004. **207**(11): p. 1941-1951 DOI: 10.1242/jeb.00973.
32. Lee, J.M., W.L. Ng, and W.Y. Yeong, *Resolution and shape in bioprinting: strategizing towards complex tissue and organ printing.* Applied Physics Reviews, 2019. **6**(1): p. 011307 DOI: 10.1063/1.5053909.
33. Guo, Z., L. An, S. Lakshmanan, J.N. Armstrong, S. Ren, and C. Zhou, *Additive Manufacturing of Porous Ceramics With Foaming Agent.* Journal of Manufacturing Science and Engineering, 2021. **144**(2): p. 021010 DOI: 10.1115/1.4051828.
34. Compton, B.G. and J.A. Lewis, *3D-printing of lightweight cellular composites.* Advanced materials, 2014. **26**(34): p. 5930-5935 DOI: 10.1002/adma.201401804.
35. Li, Y., H. Zhu, Y. Wang, U. Ray, S. Zhu, J. Dai, C. Chen, K. Fu, S.H. Jang, and D. Henderson, *Cellulose-Nanofiber-Enabled 3D Printing of a Carbon-Nanotube Microfiber Network.* Small Methods, 2017. **1**(10): p. 1700222 DOI: 10.1002/smtd.201700222.
36. Hausmann, M.K., P.A. Ruhs, G. Siqueira, J.r. Läuger, R. Libanori, T. Zimmermann, and A.R. Studart, *Dynamics of cellulose nanocrystal alignment during 3D printing.* ACS nano, 2018. **12**(7): p. 6926-6937 DOI: 10.1021/acsnano.8b02366.
37. Blaeser, A., D.F. Duarte Campos, U. Puster, W. Richtering, M.M. Stevens, and H. Fischer, *Controlling shear stress in 3D bioprinting is a key factor to balance printing resolution and stem cell integrity.* Advanced healthcare materials, 2016. **5**(3): p. 326-333 DOI: 10.1002/adhm.201500677.
38. Boularaoui, S., G. Al Hussein, K.A. Khan, N. Christoforou, and C. Stefanini, *An overview of extrusion-based bioprinting with a focus on induced shear stress and its effect on cell viability.* Bioprinting, 2020: p. e00093 DOI: 10.1016/j.bprint.2020.e00093.
39. Percoco, G., L. Arleo, G. Stano, and F. Bottiglione, *Analytical model to predict the extrusion force as a function of the layer height, in extrusion based 3D*

 

*printing.* Additive Manufacturing, 2021. **38**: p. 101791 DOI: 10.1016/j.addma.2020.101791.
40. Geng, P., J. Zhao, W. Wu, W. Ye, Y. Wang, S. Wang, and S. Zhang, *Effects of extrusion speed and printing speed on the 3D printing stability of extruded PEEK filament.* Journal of Manufacturing Processes, 2019. **37**: p. 266-273 DOI: 10.1016/j.jmapro.2018.11.023.
41. Trachtenberg, J.E., J.K. Placone, B.T. Smith, C.M. Piard, M. Santoro, D.W. Scott, J.P. Fisher, and A.G. Mikos, *Extrusion-based 3D printing of poly (propylene fumarate) in a full-factorial design.* ACS Biomaterials Science & Engineering, 2016. **2**(10): p. 1771-1780 DOI: 10.1021/acsbiomaterials.6b00026.
42. Zheng, X., C. Williams, C.M. Spadaccini, and K. Shea, *Perspectives on multi-material additive manufacturing.* Journal of Materials Research, 2021: p. 1-9 DOI: 10.1557/s43578-021-00388-y.
43. Therriault, D., S.R. White, and J.A. Lewis, *Chaotic mixing in three-dimensional microvascular networks fabricated by direct-write assembly.* Nature materials, 2003. **2**(4): p. 265-271 DOI: 10.1038/nmat863.
44. Xu, M., G.M. Gratson, E.B. Duoss, R.F. Shepherd, and J.A. Lewis, *Biomimetic silicification of 3D polyamine-rich scaffolds assembled by direct ink writing.* Soft Matter, 2006. **2**(3): p. 205-209 DOI: 10.1039/b517278k.
45. Simon, J.L., S. Michna, J.A. Lewis, E.D. Rekow, V.P. Thompson, J.E. Smay, A. Yampolsky, J.R. Parsons, and J.L. Ricci, *In vivo bone response to 3D periodic hydroxyapatite scaffolds assembled by direct ink writing.* Journal of Biomedical Materials Research Part A 2007. **83**(3): p. 747-758 DOI: 10.1002/jbm.a.31329.
46. Michna, S., W. Wu, and J.A. Lewis, *Concentrated hydroxyapatite inks for direct-write assembly of 3-D periodic scaffolds.* Biomaterials, 2005. **26**(28): p. 5632-5639 DOI: 10.1016/j.biomaterials.2005.02.040.
47. Maiti, A., W. Small, J. Lewicki, T. Weisgraber, E. Duoss, S. Chinn, M. Pearson, C. Spadaccini, R. Maxwell, and T. Wilson, *3D printed cellular solid outperforms traditional stochastic foam in long-term mechanical response.* Scientific reports, 2016. **6**(1): p. 1-9 DOI: 10.1038/srep24871.
48. Wu, A.S., W. Small IV, T.M. Bryson, E. Cheng, T.R. Metz, S.E. Schulze, E.B. Duoss, and T.S. Wilson, *3D printed silicones with shape memory.* Scientific reports, 2017. **7**(1): p. 1-6 DOI: 10.1038/s41598-017-04663-z.
49. Chortos, A., E. Hajiesmaili, J. Morales, D.R. Clarke, and J.A. Lewis, *3D printing of interdigitated dielectric elastomer actuators.* Advanced Functional Materials, 2020. **30**(1): p. 1907375 DOI: 10.1002/adfm.201907375.
50. Yunus, D.E., W. Shi, S. Sohrabi, and Y. Liu, *Shear induced alignment of short nanofibers in 3D printed polymer composites.* Nanotechnology, 2016. **27**(49): p. 495302 DOI: 10.1088/0957-4484/27/49/495302.
51. Roh, S., D.P. Parekh, B. Bharti, S.D. Stoyanov, and O.D. Velev, *3D printing by multiphase silicone/water capillary inks.* Advanced Materials, 2017. **29**(30): p. 1701554 DOI: 10.1002/adma.201701554.
52. Minas, C., D. Carnelli, E. Tervoort, and A.R. Studart, *3D printing of emulsions and foams into hierarchical porous ceramics.* Advanced Materials, 2016. **28**(45): p. 9993-9999 DOI: 10.1002/adma.201603390.
53. Li, X., X. Xu, L. Song, A. Bi, C. Wu, Y. Ma, M. Du, and B. Zhu, *High internal phase emulsion for food-grade 3D printing materials.* ACS Applied Materials & Interfaces, 2020. **12**(40): p. 45493-45503 DOI: 10.1021/acsami.0c11434.
54. Ren, B., J. Liu, Y. Wang, Y. Chen, K. Gan, Y. Rong, and J. Yang, *Hierarchical cellular scaffolds fabricated via direct foam writing using gelled colloidal particle-stabilized foams as the ink.* Journal of the American Ceramic Society, 2019. **102**(11): p. 6498-6506 DOI: 10.1111/jace.16543.

 